

# The most massive white dwarfs in the solar neighbourhood

Mukremin Kilic<sup>1</sup>, P. Bergeron,<sup>2</sup> Simon Blouin<sup>1</sup> and A. Bédard<sup>2</sup>

<sup>1</sup>Homer L. Dodge Department of Physics and Astronomy, University of Oklahoma, 440 W. Brooks St., Norman, OK, 73019, USA

<sup>2</sup>Département de Physique, Université de Montréal, C.P. 6128, Succ. Centre-Ville, Montréal, QC H3C 3J7, Canada

<sup>3</sup>Los Alamos National Laboratory, P.O. Box 1663, Mail Stop P365, Los Alamos, NM, 87545, USA

Accepted 2021 March 11. Received 2021 March 10; in original form 2021 February 4

## ABSTRACT

We present an analysis of the most massive white dwarf candidates in the Montreal White Dwarf Database 100 pc sample. We identify 25 objects that would be more massive than  $1.3 M_{\odot}$  if they had pure H atmospheres and CO cores, including two outliers with unusually high photometric mass estimates near the Chandrasekhar limit. We provide follow-up spectroscopy of these two white dwarfs and show that they are indeed significantly below this limit. We expand our model calculations for CO core white dwarfs up to  $M = 1.334 M_{\odot}$ , which corresponds to the high-density limit of our equation-of-state tables,  $\rho = 10^9 \text{ g cm}^{-3}$ . We find many objects close to this maximum mass of our CO core models. A significant fraction of ultramassive white dwarfs are predicted to form through binary mergers. Merger populations can reveal themselves through their kinematics, magnetism, or rapid rotation rates. We identify four outliers in transverse velocity, four likely magnetic white dwarfs (one of which is also an outlier in transverse velocity), and one with rapid rotation, indicating that at least 8 of the 25 ultramassive white dwarfs in our sample are likely merger products.

**Key words:** stars: evolution – white dwarfs.

## 1 INTRODUCTION

Stellar evolution theory tells us that stars with initial masses less than about  $8 M_{\odot}$  form degenerate cores and evolve into white dwarfs that are supported by electron degeneracy pressure. Chandrasekhar (1931) showed that there is an upper mass limit for a star that is supported by electron degeneracy pressure, which is roughly  $1.4 M_{\odot}$ . Takahashi, Yoshida & Umeda (2013) studied the evolution of the progenitors for electron capture supernovae, and found that when the mass interior to the helium burning shell reaches  $1.367 M_{\odot}$ , the ONe core collapses due to electron capture on  $^{24}\text{Mg}$  and  $^{20}\text{Ne}$ , leading to the formation of a neutron star (Miyaji et al. 1980; Nomoto 1987). Hence, single star evolution cannot produce white dwarfs more massive than  $1.367 M_{\odot}$ .

Population synthesis models demonstrate that a significant fraction of the massive white dwarfs above  $1 M_{\odot}$  likely form through double white dwarf mergers (Cheng et al. 2020; Temmink et al. 2020). The mergers of two CO core white dwarfs may leave behind a single massive white dwarf if the remnant's mass is below the Chandrasekhar limit (Schwab 2021, and references therein).

Ultramassive white dwarfs have been discovered serendipitously in surveys of nearby white dwarfs. GD 50 is the best example of an ultramassive white dwarf identified early on (Bergeron, Saffer & Liebert 1992). Based on *Gaia* Data Release 2 photometry and astrometry (Gaia Collaboration 2018), GD 50 is an  $M = 1.28 \pm 0.08 M_{\odot}$  white dwarf only 31 pc away from the Sun and likely a member of the AB Doradus moving group (Gagné et al. 2018). Magnetic white dwarfs PG 1658 + 441 (Schmidt et al. 1992) and RE J0317 – 853

(Barstow et al. 1995; Ferrario et al. 1997), and the nearby DA white dwarf LHS 4033 (Dahn et al. 2004) are similar, with mass estimates around  $1.3 M_{\odot}$ . Recent examples of ultramassive white dwarfs include the discoveries of a  $1.28 M_{\odot}$  white dwarf in the open cluster M37 (Cummings et al. 2016), a rapidly rotating  $\sim 1.33 M_{\odot}$  DBA white dwarf (Pshirkov et al. 2020), and a  $1.14 M_{\odot}$  white dwarf with a mixed hydrogen-carbon atmosphere (Hollands et al. 2020).

The 40 pc white dwarf sample in the Northern hemisphere includes three white dwarfs with  $\log g \geq 9$  (McCleery et al. 2020). The most massive white dwarf in that sample is WD 1653 + 256 with  $M = 1.285 \pm 0.003 M_{\odot}$ . Kilic et al. (2020) performed a detailed model atmosphere analysis of the 100 pc white dwarf sample in the SDSS footprint. With a larger survey volume, they found white dwarfs with masses up to  $1.36 M_{\odot}$ . J1140 + 2322, with  $T_{\text{eff}} = 11850 \pm 200 \text{ K}$  and  $M = 1.358 \pm 0.022$ , is the most massive white dwarf in that sample, though the more precise *Gaia* EDR3 parallax (Gaia Collaboration 2020) indicates a slightly more distant and less massive white dwarf. Both mass estimates for WD 1653+256 and J1140 + 2322 assume a CO core.

To search for the most massive white dwarfs in the solar neighbourhood, here we present a detailed model atmosphere analysis of the spectroscopically confirmed or candidate ultramassive white dwarfs in the Montreal White Dwarf Database 100 pc sample (MWDD, Dufour et al. 2017). We discuss the details of our selection of ultramassive white dwarfs, and present follow-up spectroscopy of two of the newly identified candidates in Section 2. We provide the details of our fitting method and new evolutionary calculations in Section 3. We present the model atmosphere analysis of each object in Section 4, and discuss the properties of the ultramassive white dwarf sample in Section 5, and conclude.

\* E-mail: [kilic@ou.edu](mailto:kilic@ou.edu)

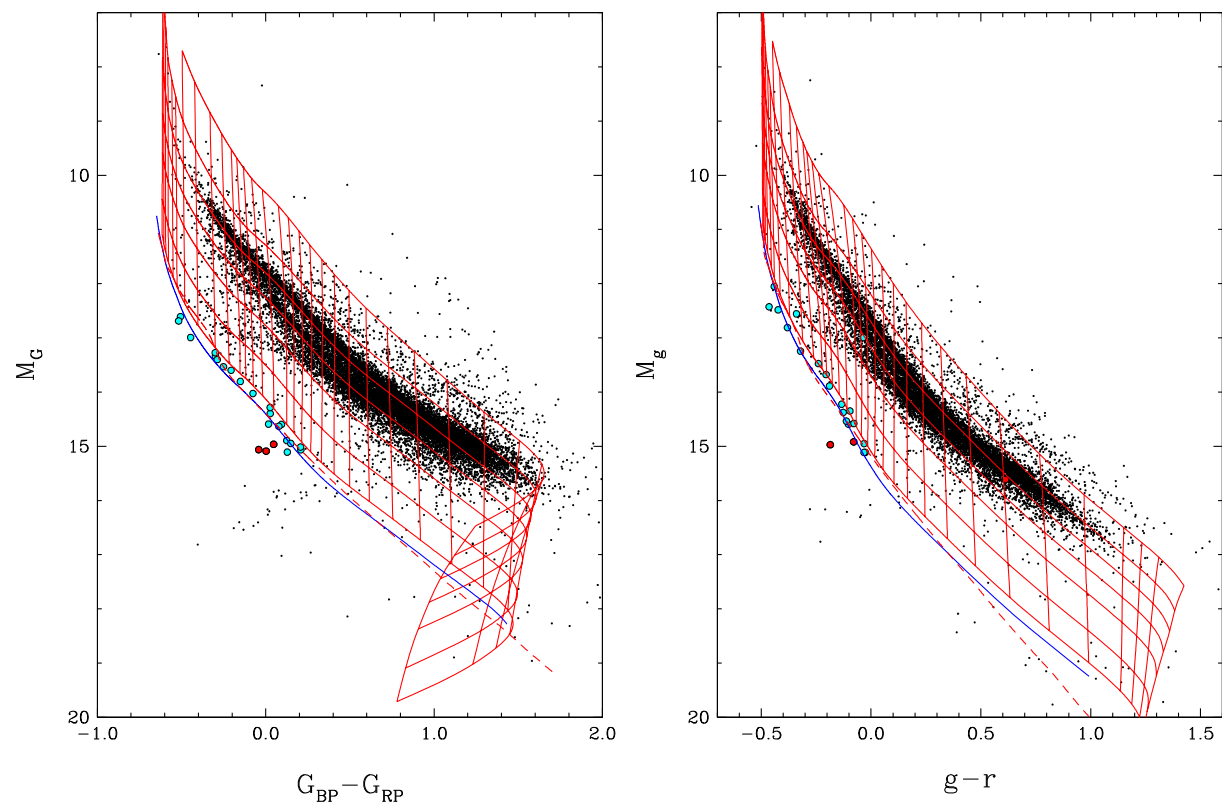


**Figure 1.** *Gaia* (left) and Pan-STARRS (right) colour-magnitude diagram of the 100 pc sample in the Montreal White Dwarf Database (Dufour et al. 2017). Red solid lines show the cooling sequences for CO core and pure H atmosphere white dwarf models with 0.2, 0.4, 0.6, 0.8, 1.0, 1.2, and 1.3  $M_{\odot}$  (from top to bottom). The dashed line shows the evolutionary sequence for 1.3  $M_{\odot}$  pure He atmosphere white dwarfs, whereas the solid blue line shows the same for 1.29  $M_{\odot}$  pure H atmosphere ONe core white dwarfs. Our ultramassive white dwarf sample and the three outliers are marked by filled cyan and red dots, respectively.

## 2 ULTRAMASSIVE WHITE DWARFS WITHIN 100 PC

### 2.1 Sample selection

We use the 100 pc white dwarf sample from the MWDD to select ultramassive white dwarf candidates. The MWDD selection is based on *Gaia* DR2 (Gaia Collaboration 2018), and includes all candidates with  $10\sigma$  significant parallax ( $\varpi$ ),  $G_{\text{BP}}$  and  $G_{\text{RP}}$  photometry, and  $\varpi + \sigma_{\varpi} > 10$  mas. To create a clean sample, non-Gaussian outliers in colour and absolute magnitude are removed using the recommendations from Lindegren et al. (2018), and a cut in *Gaia* colour and absolute magnitude is used to select the white dwarf candidates.<sup>1</sup>

Fig. 1 shows the colour-magnitude diagram of this sample in *Gaia* and Pan-STARRS (Chambers et al. 2016) filters, along with the evolutionary sequences for 0.2, 0.4, 0.6, 0.8, 1.0, 1.2, and 1.3  $M_{\odot}$  (red lines, described further in Section 3.3) CO core and 1.29  $M_{\odot}$  ONe core (blue line, Camisassa et al. 2019) white dwarfs with pure H atmospheres. The dashed line shows the 1.3  $M_{\odot}$  pure He atmosphere CO core white dwarf sequence. The main split in the white dwarf sequence due to the atmospheric composition (Bergeron et al. 2019), as well as the IR-faint (also referred to as ultracool) white dwarf sequence (Kilic et al. 2020), blue objects with  $G_{\text{BP}} - G_{\text{RP}} \sim 0$  and  $M_G \sim 16$  mag, are also clearly visible in this figure.

<sup>1</sup> See <http://montrealwhitedwarfdatabase.org/faq.html> for details.

We use these colour-magnitude diagrams to select ultramassive white dwarf candidates. Masses are estimated based on formal fits to the *Gaia* photometry and parallax. We restricted the candidates in absolute magnitude ( $M_G < 15.2$  mag) to avoid the IR-faint white dwarf sequence. The cyan symbols mark the candidates with  $M > 1.3 M_{\odot}$  according to the full photometric fits assuming CO core models. We identify 23 ultramassive white dwarf candidates based on *Gaia* data. We repeat the same experiment using Pan-STARRS photometry (the right-hand panel in Fig. 1), and identify 22 candidates, 17 of which are common to both catalogues. Hence, we identify a total of 28 candidates for further analysis.

Strikingly, three stars in this sample (marked by red dots in Fig. 1) seem to be significantly below the 1.29  $M_{\odot}$  sequence for ONe core white dwarfs in the *Gaia* colour-magnitude diagram (the left-hand panel). This is suggestive of masses significantly above 1.3  $M_{\odot}$ , and near the Chandrasekhar limit. For example, the most significant outlier in this figure, J0254 + 3019 (*Gaia* DR2 129352114170007680) would have  $M = 1.414 \pm 0.032 M_{\odot}$  based on *Gaia* parallax and photometry and pure H atmosphere CO core white dwarf models. This object is also the most significant outlier in the Pan-STARRS colour-magnitude diagram, but the Pan-STARRS photometry, which provides a broader wavelength coverage and improved constraints on the atmospheric parameters of our targets, indicates a slightly lower mass of 1.370  $M_{\odot}$  for a pure H atmosphere white dwarf.

The *Gaia* EDR3 parallax for one of these three outliers, *Gaia* DR2 6033039719166862336, puts it well beyond 100 pc. In addition, its  $G_{\text{BP}} - G_{\text{RP}}$  colour in *Gaia* DR2 is significantly different than that in

**Table 1.** Ultramassive white dwarf candidates.

Object	Source ID	Gaia DR2 $\varpi$ (mas)	Gaia EDR3 $\mu$ (mas yr $^{-1}$ )	Gaia EDR3 $V_{\tan}$ (km s $^{-1}$ )	Gaia DR2 $G$ (mag)	Gaia DR2 $G_{\text{BP}} - G_{\text{RP}}$ (mag)
SDSS J114012.81 + 232204.7	3980865789203927680	13.77 ± 0.29	62.8	21.6	18.84	+0.017
SDSS J132926.04 + 254936.4	1448232907440917760	11.59 ± 0.10	23.6	9.7	17.69	-0.446
SDSS J172736.28 + 383116.9	1343557102670161664	9.76 ± 0.31	49.1	23.9	19.95	+0.047
SDSS J180001.21 + 451724.7	2115952197141317888	11.86 ± 0.10	72.4	29.0	18.22	-0.206
SDSS J221141.80 + 113604.5	2727596187657230592	14.52 ± 0.33	172.3	56.2	19.27	+0.128
SDSS J225513.48 + 071000.9	2712093451662656256	10.82 ± 0.37	45.0	19.7	19.22	+0.036
SDSS J235232.30 - 025309.2	2448933731627261824	33.35 ± 0.08	698.7	99.3	17.00	+0.094
WD J004917.14 - 252556.81	2345323551189913600	10.04 ± 0.25	36.2	17.1	19.07	-0.076
WD J010338.56 - 052251.96	2524879812959998592	34.42 ± 0.10	176.7	24.3	17.37	+0.208
WD J025431.45 + 301935.38	12935211417007680	10.16 ± 0.43	59.1	27.6	19.80	+0.002
WD J032900.79 - 212309.24	5099116118775025408	16.98 ± 0.24	71.1	19.9	18.84	+0.149
WD J042642.02 - 502555.21	4781653099991148928	12.74 ± 0.08	26.2	9.7	18.00	-0.251
WD J043952.72 + 454302.81	253936196167057664	10.43 ± 0.14	44.9	20.4	18.27	-0.288
WD J055631.17 + 130639.78	3343720447543820672	10.85 ± 0.53	58.3	25.5	19.73	+0.207
WD J060853.60 - 451533.03	5567732956694899712	11.62 ± 0.08	70.5	28.8	18.00	-0.299
WD J070753.00 + 561200.25	988421680189764224	11.52 ± 0.13	72.8	30.0	18.00	-0.300
WD J080502.93 - 170216.57	5721057173131773184	22.44 ± 0.10	426.7	90.1	17.64	+0.027
WD J093430.71 - 762614.48	5203792030921237248	11.85 ± 0.24	79.6	31.8	19.49	+0.125
WD J095933.33 - 182824.16	5671878015177884032	16.84 ± 0.15	104.6	29.4	18.17	+0.026
WD J111646.44 - 160329.42	3559695493657381248	15.52 ± 0.20	249.9	76.3	18.65	+0.078
WD J125428.86 - 045227.48	3678497445865946624	11.11 ± 0.26	9.8	4.2	18.60	-0.151
WD J174441.56 - 203549.05	4118923497232723072	10.05 ± 0.12	83.2	39.2	17.70	-0.232
WD J181913.36 - 120856.44	4153618204302689920	19.42 ± 0.07	11.5	2.8	15.77	-0.483
WD J183202.83 + 085636.24	4479342339285057408	13.24 ± 0.10	8.7	3.1	17.05	-0.517
WD J190132.74 + 145807.18	4506869128279648512	24.15 ± 0.05	119.8	23.5	15.70	-0.507

*Gaia* EDR3 and also the Pan-STARRS  $g - r$  colour. This object is marked by the red dot in the middle of the white dwarf sequence in the Pan-STARRS colour-magnitude diagram shown in the right-hand panel of Fig. 1. We remove this object from the sample, as well as two additional objects with incomplete (1 to 3 filter) Pan-STARRS photometry, lowering our sample size to 25 objects.

Table 1 presents the observational properties of this sample. We provide the SDSS object names, if available. Otherwise, we provide the object names in the WD J format as reported in the MWDD. We also provide the most recent astrometry from *Gaia* EDR3, but avoid using EDR3 photometry since the photometric calibration has changed between DR2 and EDR3. Our sample includes targets with *Gaia*  $G$  magnitudes ranging from 15.70 to 19.95 mag, with J0254+3019 and J1727 + 3831, the two remaining outliers highlighted in Fig. 1, being the faintest.

## 2.2 Observations

We obtained follow-up optical spectroscopy of J0254+3019 and J1727 + 3831 using the 8m Gemini telescope equipped with the Gemini Multi-Object Spectrograph (GMOS) as part of the queue program GN-2020A-DD-113. We used the B600 grating and a 1" slit, providing wavelength coverage from 3670 Å to 6855 Å and a resolution of 2 Å per pixel in the  $4 \times 4$  binned mode. We obtained two 400-s exposures of J0254+3019 and two 600-s exposures of J1727 + 3831. We used the IRAF GMOS package to reduce these data.

Given the lack of any absorption lines in our relatively low signal-to-noise ratio spectrum of J0254+3019, we obtained four additional 826-s exposures as part of the program GN-2020B-FT-107. Our combined spectra from these two Gemini programs confirm the DC spectral type for J0254+3019 and DA type for J1727 + 3831.

## 3 MODEL ATMOSPHERE ANALYSIS

### 3.1 The fitting method

We use the photometric technique as described in Bergeron et al. (2019), and use the SDSS  $u$  and Pan-STARRS  $grizy$  photometry along with the *Gaia* EDR3 parallaxes to constrain the effective temperature and the solid angle,  $\pi(R/D)^2$ , where  $R$  is the radius of the star and  $D$  is its distance. With a precise distance measurement from *Gaia*, we can constrain the radius of each star directly, and therefore its mass based on the evolutionary models for a given core composition.

The details of our fitting method including the model grids used are further discussed in Bergeron et al. (2019), Genest-Beaulieu & Bergeron (2019), Blouin et al. (2019), and Kilic et al. (2020). Our model grids for both pure H and pure He atmosphere white dwarfs extend to  $\log g = 9.5$ . We supplement the pure H and pure He atmosphere model grids with mixed H/He atmosphere model grids with  $\log \text{H/He} = -5$  for stars with temperatures below 12 000 K. Three of our targets are outside of the Pan-STARRS footprint; we use *Gaia* DR2 photometry in our analysis for those stars. Since all of our targets are within 100 pc, we do not correct for reddening.

### 3.2 The core composition

The unknown core composition is the biggest uncertainty in our analysis; the mass estimates are systematically lower for the ONe core model fits compared to the CO core fits. Murai et al. (1968) demonstrated that the transition from CO to ONe core composition in white dwarfs that evolve from single stars occurs at  $1.06 M_{\odot}$ . Schwab (2021) studied the evolution of binary white dwarf merger remnants, and also found that the CO to ONe core transition occurs at a similar mass,  $M \geq 1.05 M_{\odot}$ , in single white dwarfs that formed via mergers.

Observationally, it is impossible to constrain the core composition of a given white dwarf and rule out massive CO core white dwarfs, unless they pulsate (e.g. Giambicchele et al. 2018). However, Cheng, Cummings & Ménard (2019) identify a significant cooling delay in high mass white dwarfs on the Q-branch (Gaia Collaboration et al. 2018). They suggest  $^{22}\text{Ne}$  settling in CO core white dwarfs as a potential source of extra energy in these stars. Bauer et al. (2020) confirm that the location of the Q branch over-density in the Gaia colour-magnitude diagram is compatible with CO cores, but not with ONe cores. This is based on the different crystallization temperatures of CO and ONe plasmas (see their fig. 3, and also fig. 2 from Tremblay et al. 2019). Ions in an ONe plasma have a higher charge, so they interact more strongly than those in a CO plasma and therefore freeze at a higher temperature. The location of the Q-branch over-density strongly favors CO cores even for white dwarfs more massive than  $1.05 M_{\odot}$ . Based on this, we not only adopt the CO core solutions in this study, but also present the ONe core solutions for comparison.

### 3.3 The mass–radius relation

In our fits below, we use detailed mass–radius relations of CO core ( $X_C = X_O = 0.5$ ) models (Bédard et al. 2020) with masses in the range  $M = 0.2–1.3 M_{\odot}$  by steps of  $0.05 M_{\odot}$ , and with thick ( $q_H \equiv M_H/M_{\star} = 10^{-4}$ ) and thin ( $q_H = 10^{-10}$ ) H layers to fit the H- and He-atmosphere white dwarfs in our sample, respectively. For the purpose of this analysis, we also calculated models at  $M = 1.334 M_{\odot}$ , which corresponds to the highest possible mass given the high-density limit of our equation-of-state tables ( $\rho = 10^9 \text{ g cm}^{-3}$ ). We also rely on the ONe core, H-rich ( $q_H \sim 10^{-6}$ ) and H-deficient ( $q_H = 0$ ) models from Camisassa et al. (2019) at  $M = 1.10, 1.16, 1.22$ , and  $1.29 M_{\odot}$  to fit the H- and He-atmosphere white dwarfs, respectively.

We first consider the effects of core composition, stellar mass, surface composition, and thickness of the H layer on the predicted colours in the colour-magnitude diagram. Fig. 2 presents a zoomed-in version of the *Gaia* colour-magnitude diagram previously displayed in Fig. 1. Coloured symbols mark our ultramassive white dwarf sample presented in Table 1, along with the two outliers shown as red points. Note that one of our Pan-STARRS selected targets, J1744–2035, appears redder than the  $1.20 M_{\odot}$  cooling sequence based on *Gaia* DR2 photometry. However, improved constraints from Pan-STARRS photometry clearly indicate that this is an  $M \sim 1.3 M_{\odot}$  white dwarf (see Section 4.4).

Fig. 2 includes cooling sequences obtained from some of the CO and ONe core models discussed above (shown as red and blue lines, respectively). Calculations are shown for various masses indicated in the figure (less massive models are more luminous). Also shown for the most massive sequences are the results for pure H atmospheres (assuming thick H layers; solid lines) and for pure He atmospheres (assuming thin H layers for CO core models, or the H-deficient ONe core models from Camisassa et al.; dashed lines); the small effect of using thick or thin H layers for pure H atmospheres is also illustrated for the CO-core models at  $M = 1.334 M_{\odot}$  (thick and thin red solid lines, respectively). In this diagram, the CO and ONe core sequences for pure H atmospheres near  $M \sim 1.2 M_{\odot}$  can be used to estimate the effects of the core composition, with the CO core models being more luminous due to their larger radii at a given effective temperature. Interestingly enough, the CO-core sequence at  $1.334 M_{\odot}$  overlaps almost perfectly with the ONe core sequence at  $1.29 M_{\odot}$  in this colour-magnitude diagram. However, the results for the pure He atmospheres for the same masses, which rely on the CO-core thin H models or the ONe core H deficient models, are quite

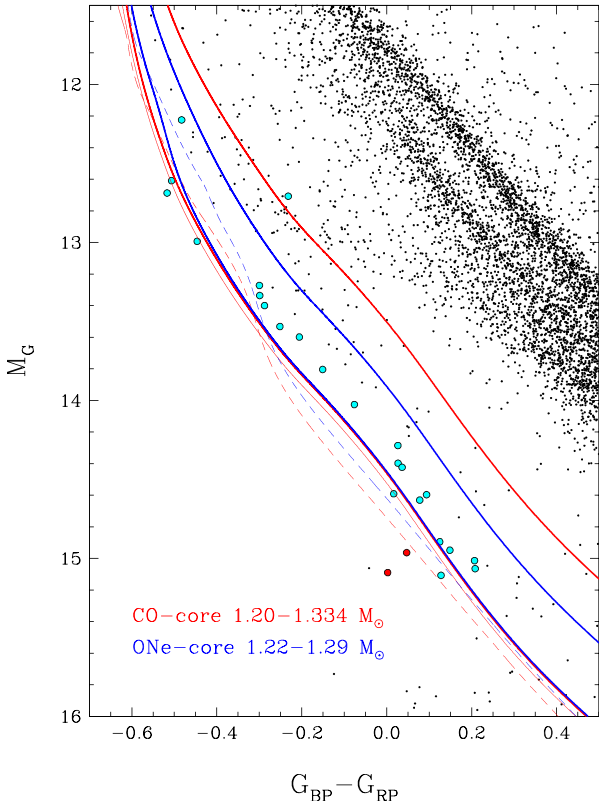


**Figure 2.** Colour-magnitude diagram of the white dwarfs in the MWDD within 100 pc (coloured symbols are discussed in the text) together with theoretical cooling sequences with CO (red) and ONe (blue) cores. The masses of the sequences are indicated in the figure; less massive sequences are more luminous. The most massive sequences for each core composition are shown for pure H (solid lines) and pure He (dashed lines) model atmospheres. Also displayed for the  $1.334 M_{\odot}$ , pure H atmospheres, CO core models, are the results for thick ( $q_H = 10^{-4}$ , thick red solid line) and thin ( $q_H = 10^{-10}$ , thin red solid line) H layers.

distinct (note that the colours calculated using CO core models with no hydrogen at all would overlap perfectly with our thin H models).

We can gain more insight into this behaviour by examining the results displayed in Fig. 3 where we show the stellar radius as a function of effective temperature for the same models illustrated in Fig. 2, for both thick and thin H layers (or H deficient in the case of the ONe core models). For the  $M \sim 1.2 M_{\odot}$  models, one can see the larger radii of the CO core models with respect to the ONe core models, as expected. The effect of the hydrogen layer mass at high temperatures is also consistent in both sets of models (the presence of hydrogen yields a larger radius at a given temperature); note that our CO-core models have hydrogen layers that are 100 times thicker than in the ONe core models. The effects of H in our CO core models are thus more pronounced. Also observed for the  $M = 1.22$  and  $1.29 M_{\odot}$  ONe core models is a drop in the stellar radius due to phase separation upon crystallization (see also fig. 11 of Camisassa et al. 2019). This drop in radius occurs at lower effective temperatures and with a smaller amplitude in H-deficient models. The net result is that at lower temperatures, the H-deficient ONe core models have larger radii than their thick H counterparts, in contrast with our CO-core models where phase separation is neglected. The effects are even more pronounced in the most massive CO-core and ONe core models displayed in Fig. 3. Here the thick H layer, CO-core

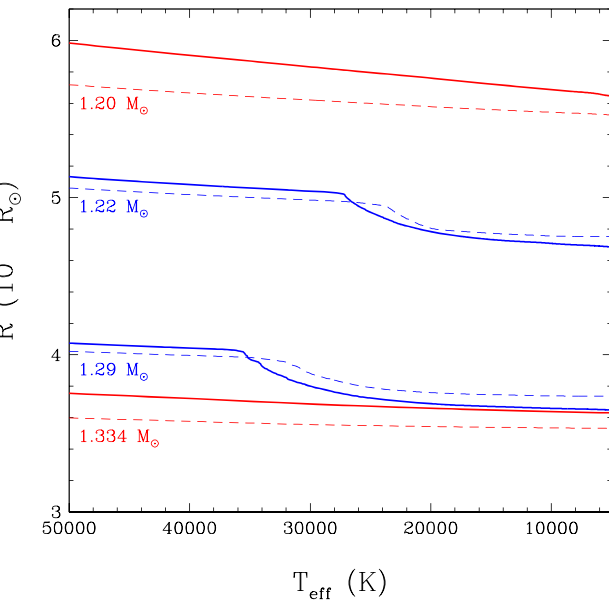


**Figure 3.** Stellar radius as a function of effective temperature for CO core (red line) and ONe core (blue line) white dwarf models with masses indicated in the figure. The solid and dashed lines correspond respectively to H-rich models ( $q_H = 10^{-4}$  for CO core and  $\sim 10^{-6}$  for ONe core models, respectively) and H-poor models ( $q_H = 10^{-10}$  for CO core and no hydrogen for ONe core models, respectively).

models at  $1.334 M_{\odot}$  overlap almost perfectly with the ONe core models at  $1.29 M_{\odot}$  below  $T_{\text{eff}} \sim 30,000$  K, while the thin H (or H deficient) models yield stellar radii that differ significantly in the same temperature range, thus explaining the particular behaviour observed in the colour-magnitude diagram displayed in Fig. 2 for the most massive sequences.

Finally, we note that both the CO-core and ONe core models are able to encompass most of the massive white dwarfs in our sample displayed in Fig. 2, in particular if we take into account the effect of atmospheric composition. The only exceptions are the three red objects identified in the figure.

## 4 RESULTS

### 4.1 SDSS J172736.28 + 383116.9

Fig. 4 shows our model fits to SDSS J172736.28 + 383116.9, hereafter J1727 + 3831, one of the outliers in the *Gaia* colour-magnitude diagram. The Pan-STARRS photometry puts this object closer to the  $1.3 M_{\odot}$  models (see Fig. 1). The top panel shows the GALEX NUV, SDSS  $u$ , and Pan-STARRS  $griz$  photometry (error bars) along with the predicted fluxes from the best-fitting pure H (filled dots) and mixed H/He (open circles) atmosphere models. The GALEX photometry is not used in the fitting, and is shown in red here and in the following figures, but it is useful for inferring the atmospheric composition in some cases. The labels in the same panel give the *Gaia* DR2 Source ID, object name, and the photometry used in the fitting. The bottom panel shows the observed Gemini spectrum (black line) along with the predicted spectrum based on the pure H solution. Note that we do not fit the spectroscopy data here. Instead, we simply over-plot the predicted Balmer line profile (red line) from the photometric fit to see if a given spectrum is consistent with a pure H atmosphere composition.

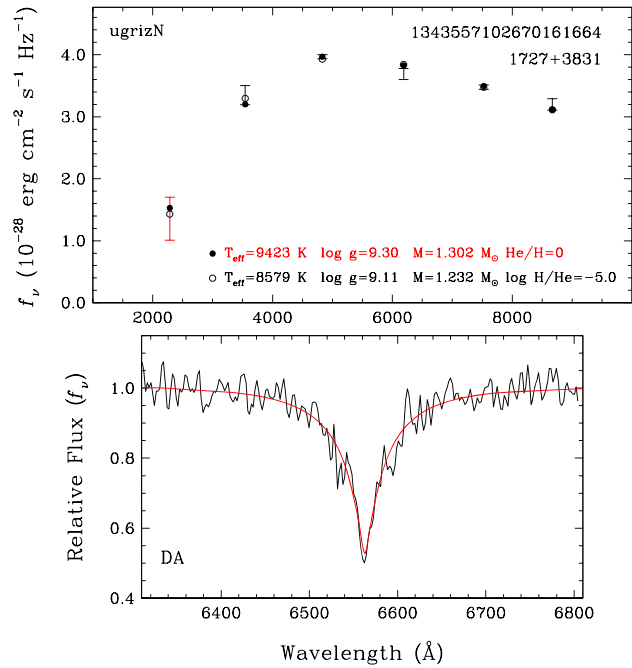


**Figure 4.** Model fits to an ultramassive white dwarf candidate observed at Gemini. The top panel shows the best-fitting H (filled dots) and He (open circles) atmosphere white dwarf models to the photometry (error bars), and includes the *Gaia* DR2 Source ID, object name, and the photometry used in the fitting:  $ugrizN$  means SDSS  $u$  + Pan-STARRS  $griz$ , and Galex NUV. The atmospheric parameters of the favored solution is highlighted in red. Here, and in the following figures, we show the model parameters for CO core white dwarfs. The bottom panel shows the observed spectrum (black line) along with the predicted spectrum (red line) based on the pure H atmosphere solution.

We cannot distinguish between the H- or He-dominated solution for J1727 + 3831 based on the photometry alone. However, the observed Gemini spectrum is clearly that of a DA-type star, and our photometric analysis indicates  $T_{\text{eff}} = 9420 \pm 200$  K and  $M = 1.302 \pm 0.011 M_{\odot}$  for a pure H atmosphere white dwarf with a CO core. The predicted H $\alpha$  line profile for these parameters provides an excellent match to the observed spectrum. Without additional information, there is no way to know the core composition. If J1727 + 3831 has an ONe core instead, its mass would be 0.05  $M_{\odot}$  lower.

### 4.2 WD J025431.45 + 301935.38

Fig. 5 shows our model fits to WD J025431.45 + 301935.38, hereafter J0254 + 3019, the most significant outlier in our sample. Even though Pan-STARRS photometry and *Gaia* EDR3 parallax indicate a mass as high as  $1.37 M_{\odot}$  for a pure H composition, it turns out that J0254 + 3019 is a DC white dwarf with no visible absorption features in its spectrum. Hence, its atmosphere is clearly not dominated by H, and it appears to be an outlier in the colour-magnitude diagrams because of its atmospheric composition.

He I lines disappear below about 11 000 K, which means that pure He atmosphere white dwarfs would appear as DC white dwarfs below this temperature. However, Bergeron et al. (2019) demonstrated that pure He atmosphere white dwarfs are extremely rare or nonexistent in the 6000–11 000 K temperature range. Reasonable mass estimates for DC white dwarfs in this temperature range require additional

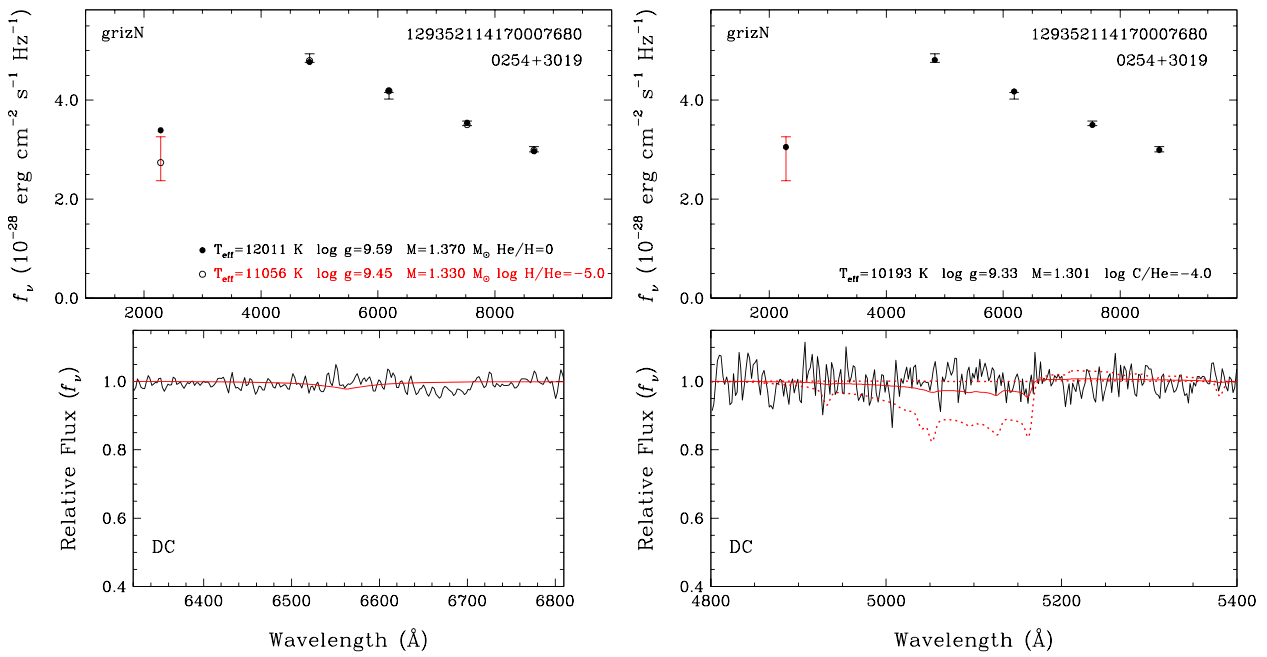


**Figure 5.** Model fits to J0254+3019, our second target observed at Gemini. The lack of any absorption features in its Gemini spectrum complicates our analysis of J0254+3019. The left-hand panels show our analysis assuming pure H- and He-rich models with trace amounts of H (similar to Fig. 4), whereas the right-hand panels show the results assuming an He-rich composition with trace amounts of C. In the lower panel, the red solid line corresponds to the model spectrum obtained from our photometric solution assuming a carbon abundance of  $\log C/He = -4$ , displayed in the upper panel, while the dotted lines show the predicted spectra assuming abundances of  $\log C/He = -3$  and  $-5$ . Depending on the unknown abundances of H and C in the atmosphere, J0254+3019 has a mass of  $1.30-1.33 M_{\odot}$ , assuming a CO core.

electron donors like hydrogen and carbon (or other metals). Given the unknown atmospheric composition, we explore both possibilities for J0254+3019.

The left-hand panels in Fig. 5 show our model atmosphere analysis using pure H and mixed H/He models with  $\log H/He = -5$ . The top left-hand panel shows our photometric fits, which indicate  $T_{\text{eff}} = 11060 \pm 560$  K and  $M = 1.330 \pm 0.016 M_{\odot}$  for a mixed H/He atmosphere and a CO core. The bottom left-hand panel compares the predicted H $\alpha$  line profile for this solution to the observed spectrum. We can clearly rule out H abundances greater than this limit, as we would have detected an H $\alpha$  line. For an ONe core, the mass estimate goes down to  $1.302 M_{\odot}$ .

The right-hand panels in Fig. 5 show the results from our analysis for an He atmosphere white dwarf with trace amounts of carbon. As discussed by Dufour, Bergeron & Fontaine (2005), the physical parameters of DQ white dwarfs determined from the photometric method are particularly sensitive to the assumed carbon abundance. In particular, fig. 8 of Dufour et al. (2005) shows that the effective temperature and stellar mass can be significantly overestimated if pure He models are used instead of models that include carbon. In this case, the presence of carbon, in addition to producing strong atomic and molecular absorption features, also contributes to increase in the number of free electrons, and thus the He $^-$  free-free opacity, particularly in the continuum forming region, resulting in lower derived photometric temperatures. Since larger solid angles  $-\pi(R/D)^2$  are required to fit the photometric data, this implies larger derived stellar radii or smaller masses. Note that a similar reasoning can be applied in the context of metal-rich DZ stars (see e.g. Dufour et al. 2007), except at very low temperatures (Blouin et al. 2018).

Our photometric fits for J0254+3019, displayed in the right-hand panels of Fig. 5, using DQ models assuming various carbon

abundances ( $\log C/He = -5, -4$ , and  $-3$ ) are consistent with the picture described above. Namely, the derived effective temperatures and stellar masses are always smaller than the values obtained from pure He models. However, our results also revealed that the lower the assumed carbon abundance (in the range explored here), the further away our solution was from the pure He solution! To understand this peculiar trend better, we computed additional models with a range of carbon abundances, the results of which are displayed in Fig. 6. By reducing further the carbon abundance below  $\log C/He = -5$ , we gradually recover the pure He solution. The molecular Swan bands are undetectable at  $\log C/He = -5$  (see Fig. 5), which implies that invisible traces of carbon can still have a large effect on the temperature structure, and thus on the derived physical parameters.

We attempted to isolate which of the effects produced by carbon – in terms of the equation-of-state or the opacity – account for the results displayed in Fig. 6. For instance, we also show in Fig. 6 (open circles) the results obtained from model atmospheres of DQ stars where the carbon line and molecular opacities have been turned off. While the difference in temperature between the  $\log C/He = -5$  and  $-2$  solutions has been significantly reduced, the derived photometric temperatures still show a nonmonotonic variation as a function of the carbon abundance, indicating a complex interplay between the effects produced by carbon, both in terms of the equation-of-state and the opacity calculations.

The strongest carbon features are expected in the 5000–5200 Å range, and the lack of any significant features in our Gemini spectrum limits the carbon abundance to  $\log C/He \leq -4$ . If J0254+3019 has trace amounts of carbon in its atmosphere, then the best-fitting mass would be  $1.301 \pm 0.014 M_{\odot}$  for a CO core, and  $1.261 \pm 0.016 M_{\odot}$  for an ONe core. Hence, depending on the unknown atmospheric and core composition, J0254+3019 has a mass in the range  $1.26-1.33 M_{\odot}$ .

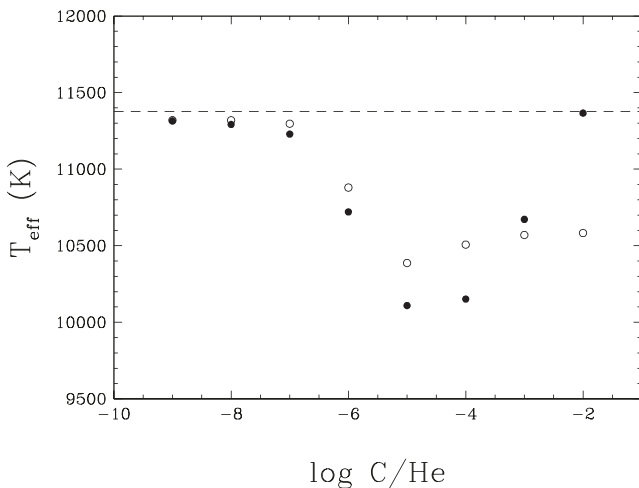


**Figure 6.** Effective temperature determined from photometric fits to J0254 + 3019 as a function of the assumed carbon abundance (filled circles). The dashed line indicates the temperature obtained from fits using pure He atmospheres. Similar results obtained using DQ model atmospheres where the carbon line and molecular opacities have been omitted are shown by open circles.

Coutu et al. (2019) presented an analysis of the DQ white dwarfs in the MWDD, and showed that massive DQ white dwarfs hotter than 10 000 K have carbon abundances of  $\log C/\text{He} > -4$ . We can safely rule out such a carbon abundance in J0254 + 3019, and it is unlikely that J0254 + 3019 belongs to the massive DQ white dwarf population. Hence, the mixed H/He atmosphere solution discussed above is probably more representative of the physical parameters of this star.

### 4.3 Additional targets with follow-up optical spectroscopy

#### 4.3.1 DA white dwarfs

There are eight additional targets in our sample with follow-up spectroscopy available in the literature: four have spectra in the SDSS, and four others have spectra presented in Deacon et al. (2009, IPHAS J190132.77 + 145807.6), Gianninas, Bergeron & Ruiz (2011, LHS 4033), Tremblay et al. (2020, G270-126), and Pshirkov et al. (2020, J1832 + 0856). These include five DA white dwarfs, two of which are magnetic, one DBA, and two DC white dwarfs.

Fig. 7 shows our model atmosphere analysis for the three non-magnetic DAs in our sample. The symbols and the panels are the same as in Fig. 4, but we show an additional panel at the bottom to display a broader wavelength range for each object. These three stars have the entire set of Galex FUV and NUV, SDSS *u*, and Pan-STARRS *grizy* photometry available, which enable precise constraints on their temperatures, radii, and therefore masses. The photometric solutions provide an excellent match to the observed H line profiles, demonstrating that they have pure H atmospheres.

J2352 – 0253 (LHS 4033, the right-hand panels) is one of the best-studied ultramassive white dwarfs in the literature. Dahn et al. (2004) used both the photometric and spectroscopic method to demonstrate that this is an extremely massive white dwarf. They used the photometric technique with a ground-based parallax measurement from the USNO to derive  $T_{\text{eff}} = 10,900 \pm 290$  K and  $M = 1.31 - 1.33 M_{\odot}$ , depending on the core composition. Dahn et al. (2004) had access to evolutionary models up to only  $1.2 M_{\odot}$ , and they adopted the Hamada & Salpeter (1961) mass–radius relation for both the spectroscopic and photometric techniques. Hence, our

analysis supersedes the results presented there. Nevertheless, our estimates of  $T_{\text{eff}} = 10680 \pm 100$  K and  $M = 1.319 \pm 0.003 M_{\odot}$  under the assumption of a CO core are entirely consistent with the results from Dahn et al. (2004).

The other DA white dwarfs in this figure, J1140+2322 and J1329 + 2549, are both hotter and more massive. The best-fitting mass estimates for CO cores are  $M = 1.336 \pm 0.006 M_{\odot}$  and  $1.351 \pm 0.006 M_{\odot}$ , respectively. Both of these measurements are above the highest mass CO core model available ( $1.334 M_{\odot}$ ), and thus they are extrapolated and should be used with caution.

Table 2 presents the physical parameters of all 10 ultramassive white dwarfs with follow-up spectroscopy available, including these three DA white dwarfs. The best-fitting temperatures do not depend on the core composition, but the masses and the cooling ages do. For completeness, we provide the masses and the cooling ages for both ONe and CO core compositions in Table 2.

#### 4.3.2 Magnetic white dwarfs and others

The left-hand panels in Fig. 8 show our model atmosphere analysis for the magnetic DA white dwarf J2211 + 1136, which shows a weak H $\alpha$  line. Since we do not model the magnetic field structure, our best-fitting pure H solution does not match the H $\alpha$  line profile. Regardless, this is clearly a DA white dwarf, and our analysis indicates a mass of  $1.310 \pm 0.008 M_{\odot}$  for a CO core.

IPHAS J190132.77 + 145807.6 (middle panels in Fig. 8) was classified as a DC white dwarf by Deacon et al. (2009) since it does not show any significant features in its optical spectrum. However, it is too hot to be truly a DC white dwarf, as H or He lines should be visible at a surface temperature near 30 000 K. Hence, it must be a magnetic white dwarf, either a DAH or a DBH. Regardless of the atmospheric composition, J1901 + 1458 is clearly a very massive white dwarf with  $M = 1.319 \pm 0.004 M_{\odot}$  (pure H solution) or  $1.330 \pm 0.003 M_{\odot}$  (pure He solution) for a CO core.

Similarly, J2255+0710 (right-hand panels) has a DC-like spectrum, but there are some weak features, including a broad unidentified absorption feature near 4130 Å. Hence, J2255 + 0710 is likely magnetic as well. Depending on the atmospheric composition, its mass is in the range  $1.22 - 1.30 M_{\odot}$  for a CO core.

There are two additional targets with follow-up spectroscopy available in the literature. The first one, J0103–0522, is DAH: white dwarf included in the 40 pc sample of Tremblay et al. (2020). The remaining target, J1832 + 0856, is a rapidly rotating DBA white dwarf (Pshirkov et al. 2020). Our analysis using pure He atmosphere models for this object results in  $T_{\text{eff}} = 34200 \pm 1020$  K and  $M = 1.319 \pm 0.004 M_{\odot}$ , assuming a CO core.

### 4.4 Objects with unknown spectral types

Fig. 9 shows the spectral energy distributions and our model atmosphere fits to 15 ultramassive white dwarfs with no follow-up spectroscopy available in the literature. Even though the presence or lack of a Balmer jump between the UV and optical filters can be used to distinguish between the H- and He-atmosphere solutions, we refrain from assigning composition based on photometry alone. However, we note that there are several objects with spectral energy distributions that are best explained by H-dominated atmospheres: J0049 – 2525, J0707 + 5612, J0959 – 1828, J1116 – 1603, J1254 – 0452, and J1800 + 4517 have SDSS *u* or GALEX UV data that clearly favour the pure H atmosphere solution. On the other hand, J0426 – 5025 and J0805 – 1702 have UV photometry that favour He-dominated atmospheres.

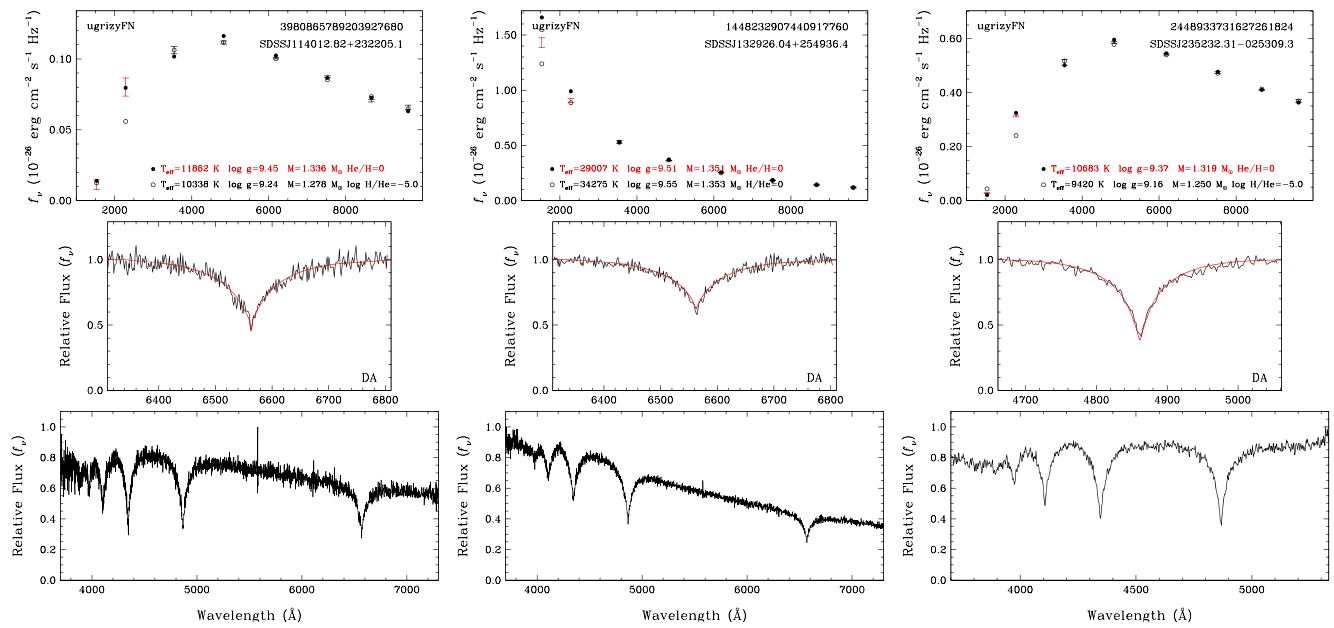


**Figure 7.** Model atmosphere fits to three ultramassive DA white dwarfs with spectroscopy available in the literature. The symbols and the panels are the same as in Fig. 4, except that the bottom panels show a broader wavelength range for each object.

**Table 2.** Physical parameters of the spectroscopy sample assuming ONe or CO cores. All solutions above  $1.29 M_{\odot}$  for ONe core models and above  $1.334 M_{\odot}$  for CO core models are extrapolated.

Object	Composition	Spectral type	$T_{\text{eff}}$ (K)	ONe core Mass ( $M_{\odot}$ )	ONe core Cooling age (Gyr)	CO core Mass ( $M_{\odot}$ )	CO core Cooling age (Gyr)
J010338.56 – 052251.96	H	DAH:	$9040 \pm 70$	$1.262 \pm 0.003$	$2.84 \pm 0.03$	$1.310 \pm 0.003$	$2.60 \pm 0.04$
J025431.45 + 301935.38	$\log H/He = -5$	DC	$11060 \pm 560$	$1.302 \pm 0.024$	$2.25 \pm 0.10$	$1.330 \pm 0.016$	$1.49 \pm 0.17$
...	$\log C/He = -4$	DC	$10190 \pm 290$	$1.261 \pm 0.016$	$2.53 \pm 0.08$	$1.301 \pm 0.014$	$1.93 \pm 0.12$
J114012.81 + 232204.7	H	DA	$11860 \pm 220$	$1.294 \pm 0.008$	$2.10 \pm 0.04$	$1.336 \pm 0.006$	$1.71 \pm 0.06$
J132926.04 + 254936.4	H	DA	$29010 \pm 750$	$1.314 \pm 0.006$	$0.81 \pm 0.05$	$1.351 \pm 0.006$	$0.37 \pm 0.03$
J172736.28 + 383116.9	H	DA	$9420 \pm 200$	$1.252 \pm 0.012$	$2.78 \pm 0.08$	$1.302 \pm 0.011$	$2.59 \pm 0.12$
J183202.83 + 085636.24	He	DBA	$34210 \pm 1020$	$1.301 \pm 0.006$	$0.45 \pm 0.03$	$1.319 \pm 0.004$	$0.20 \pm 0.02$
J190132.74 + 145807.18	H	DC	$29100 \pm 480$	$1.279 \pm 0.003$	$0.61 \pm 0.02$	$1.319 \pm 0.004$	$0.35 \pm 0.02$
...	He	DC	$37070 \pm 720$	$1.318 \pm 0.004$	$0.40 \pm 0.01$	$1.330 \pm 0.003$	$0.14 \pm 0.01$
J221141.80 + 113604.5	H	DAH	$9020 \pm 160$	$1.262 \pm 0.009$	$2.85 \pm 0.07$	$1.310 \pm 0.008$	$2.61 \pm 0.11$
J225513.48 + 071000.9	H	DC	$10990 \pm 210$	$1.252 \pm 0.012$	$2.36 \pm 0.05$	$1.302 \pm 0.011$	$2.18 \pm 0.09$
...	$\log H/He = -5$	DC	$9530 \pm 170$	$1.188 \pm 0.014$	$2.88 \pm 0.06$	$1.216 \pm 0.018$	$2.48 \pm 0.07$
J235232.30 – 025309.2	H	DA	$10680 \pm 100$	$1.272 \pm 0.003$	$2.38 \pm 0.02$	$1.319 \pm 0.003$	$2.10 \pm 0.03$

We provide both H- and He-dominated fits for each object in this figure, and list the best-fitting parameters for each composition in Table 3. All of these targets have  $M \leq 1.344 M_{\odot}$  assuming CO core composition. Note that two objects, J0556+1306 and J0707+5612, have mass estimates below  $1.3 M_{\odot}$  for the CO-core solutions. These two targets were selected as  $M \geq 1.3 M_{\odot}$  white dwarfs based on *Gaia* photometry. However, our improved fits using *Gaia* EDR3 parallax and Pan-STARRS photometry indicate masses slightly below this limit.

## 5 DISCUSSION

### 5.1 The most massive white dwarf in the solar neighbourhood

By performing a detailed model atmosphere analysis of the MWDD 100 pc sample, we tried to identify the most massive white dwarfs in the solar neighbourhood. Among the 10 objects with follow-up

optical spectroscopy available, there are two objects with masses above  $1.334 M_{\odot}$ , the highest mass CO core model currently available. Hence, their mass estimates are extrapolated, and therefore uncertain. With that caveat in mind, the DA white dwarf J1329 + 2549 is currently the most massive white dwarf known in the solar neighbourhood with well-constrained atmospheric parameters and a mass of  $1.351 \pm 0.006 M_{\odot}$ .

Kilic et al. (2020) estimated a mass of  $1.358 \pm 0.022 M_{\odot}$  for the DA white dwarf J1140 + 2322, which is also included in our sample. However, the previous analysis on this object was based on the *Gaia* DR2 parallax measurement and also limited to CO core models up to  $1.2 M_{\odot}$ . Based on evolutionary sequences extended up to  $1.334 M_{\odot}$  and the *Gaia* EDR3 parallax measurement, which implies a slightly larger distance, we derive a mass of  $1.336 \pm 0.006 M_{\odot}$  for J1140 + 2322, making it the second most massive white dwarf in our spectroscopy sample.

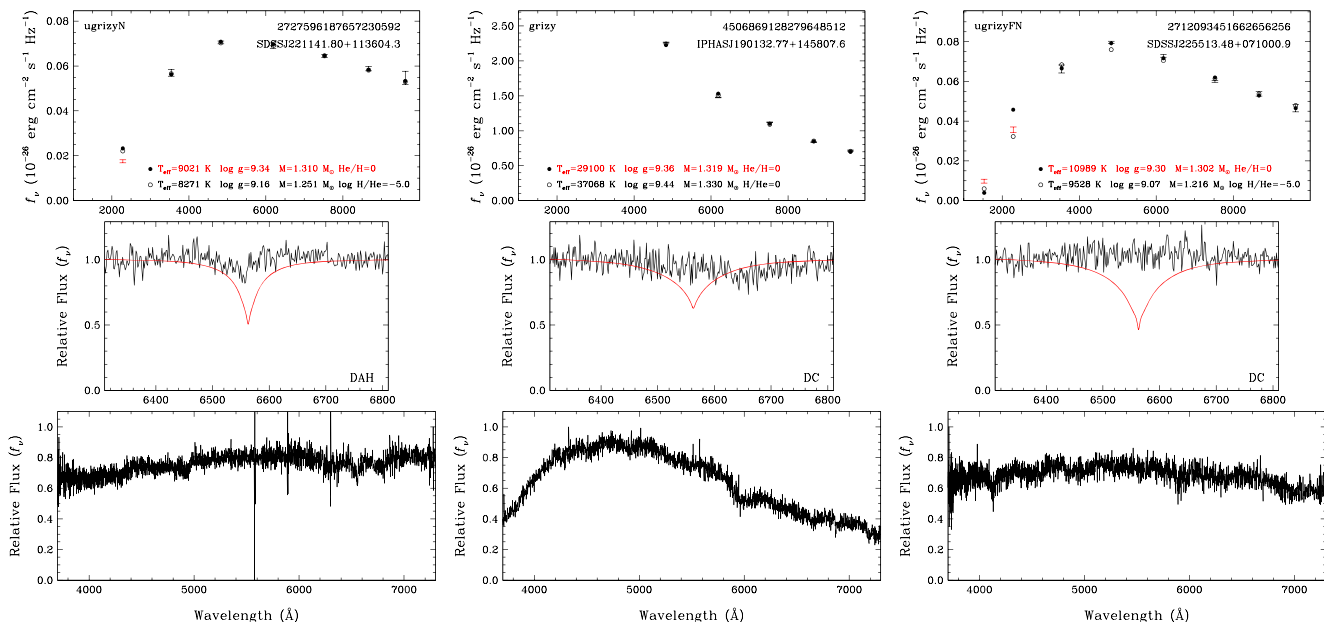


**Figure 8.** Model atmosphere fits to three magnetic white dwarf candidates with spectroscopy available in the literature. The symbols and the panels are the same as in Fig. 7. Note that J1901 + 1458 spectrum is not flux-calibrated.

The MWDD sample selection is optimized for creating a clean white dwarf sample rather than completeness. Searching the *Gaia* DR2 white dwarf catalogue of Gentile Fusillo et al. (2019) for  $M \geq 1.3 M_{\odot}$  objects within 100 pc reveals 40 high probability candidates with masses up to  $1.37 M_{\odot}$  under the assumption of a pure H atmosphere and a CO core. These mass estimates are based on *Gaia* DR2 photometry and parallaxes. Three of these systems did not make it into the clean candidate selection in the MWDD. Of the remaining 37 targets, 19 are included in our sample and in Table 1, but the remaining 18 are excluded because they appear less massive or because of our colour and magnitude selection avoiding the IR-faint white dwarf sequence.

Among the 18 excluded objects, six have follow-up spectroscopy available in the literature. Three of these, *Gaia* DR2 2533306985471073920, 601566038739612160, 1358301480583401728, are in the SDSS footprint, and additional analysis by Kilic et al. (2020) using *Gaia* parallax and SDSS + Pan-STARRS photometry showed that their masses are below  $1.3 M_{\odot}$ . Another object, SDSS J071816.41 + 373139.1, could be included in our list of ultramassive white dwarfs if it has an He-dominated atmosphere. The best-fitting He-dominated atmosphere solution has  $T_{\text{eff}} = 40636 \pm 1506$  K and  $M = 1.316 \pm 0.008 M_{\odot}$  (Kilic et al. 2020). However, we do not expect to see a DC white dwarf at such a high temperature, unless it is a magnetic DBH or DAH; its atmospheric composition is uncertain. The pure H solution implies a mass below  $1.3 M_{\odot}$ . Hence, it is not surprising that it is excluded from our list of 25 ultramassive white dwarfs presented in Table 1. Two additional objects, J1001+3903 and J1337 + 0001 (Harris et al. 2001; Gates et al. 2004), are spectroscopically confirmed IR-faint (ultracool) white dwarfs.

In summary, we are confident that we are not missing a large population of  $M \geq 1.3 M_{\odot}$  ultramassive white dwarfs within the *Gaia* 100 pc sample. However, *Gaia* itself is missing a number of cool ultramassive white dwarfs, since such white dwarfs disappear quickly below *Gaia*'s  $G = 20$  mag detection limit (Bergeron et al. 2019; Kilic et al. 2020).

## 5.2 Single stars versus mergers

A large fraction of the ultramassive white dwarfs in our sample have likely formed as a result of binary mergers. Based on population synthesis calculations, Temmink et al. (2020) suggest that around 30 to 50 per cent of single white dwarfs with  $M > 0.9 M_{\odot}$  form through a binary merger.

Merger populations can reveal themselves through their kinematics. Since merger systems would be found in older populations that are kinematically heated up, they should show a higher velocity dispersion compared to a population of single stars (Wegg & Phinney 2012). For example, studying the transverse velocity distribution of a large sample of  $M = 0.8 - 1.3 M_{\odot}$  white dwarfs, Cheng et al. (2020) show that 20 per cent of the massive white dwarfs in their sample must come from mergers. Similarly, Kilic et al. (2020) found that 10 of their 44 hot DA white dwarfs with  $M > 1 M_{\odot}$  have transverse velocities in excess of  $50 \text{ km s}^{-1}$ , indicating a merger origin.

Fig. 10 shows the *Gaia* colours and tangential velocities of our sample of 25 ultramassive white dwarfs presented in Table 1. Excluding the  $3\sigma$  outliers, the average tangential velocity of the sample is  $21 \pm 10 \text{ km s}^{-1}$ , which is consistent with a young disk population. There are four objects with transverse velocities (see Table 1) that are significantly higher than expected,  $> 50 \text{ km s}^{-1}$ , for their cooling ages. These include the DA white dwarfs J2211 + 1136 (which is also magnetic) and J2352 – 0253 (LHS 4033), and two additional objects without follow-up spectroscopy, J0805 – 1702 and J1116 – 1603. Hence, these four ultramassive white dwarfs likely formed through mergers.

Merger populations can also reveal themselves through magnetism. A magnetic dynamo can be generated during a merger event though differential rotation within a common-envelope or an accretion disk (Briggs et al. 2015). Tout et al. (2008) suggest that all highly magnetic white dwarfs, either found as single stars or as components of magnetic cataclysmic variables, have a binary origin (but see Caiazzo et al. 2020). Briggs et al. (2015) further argue that

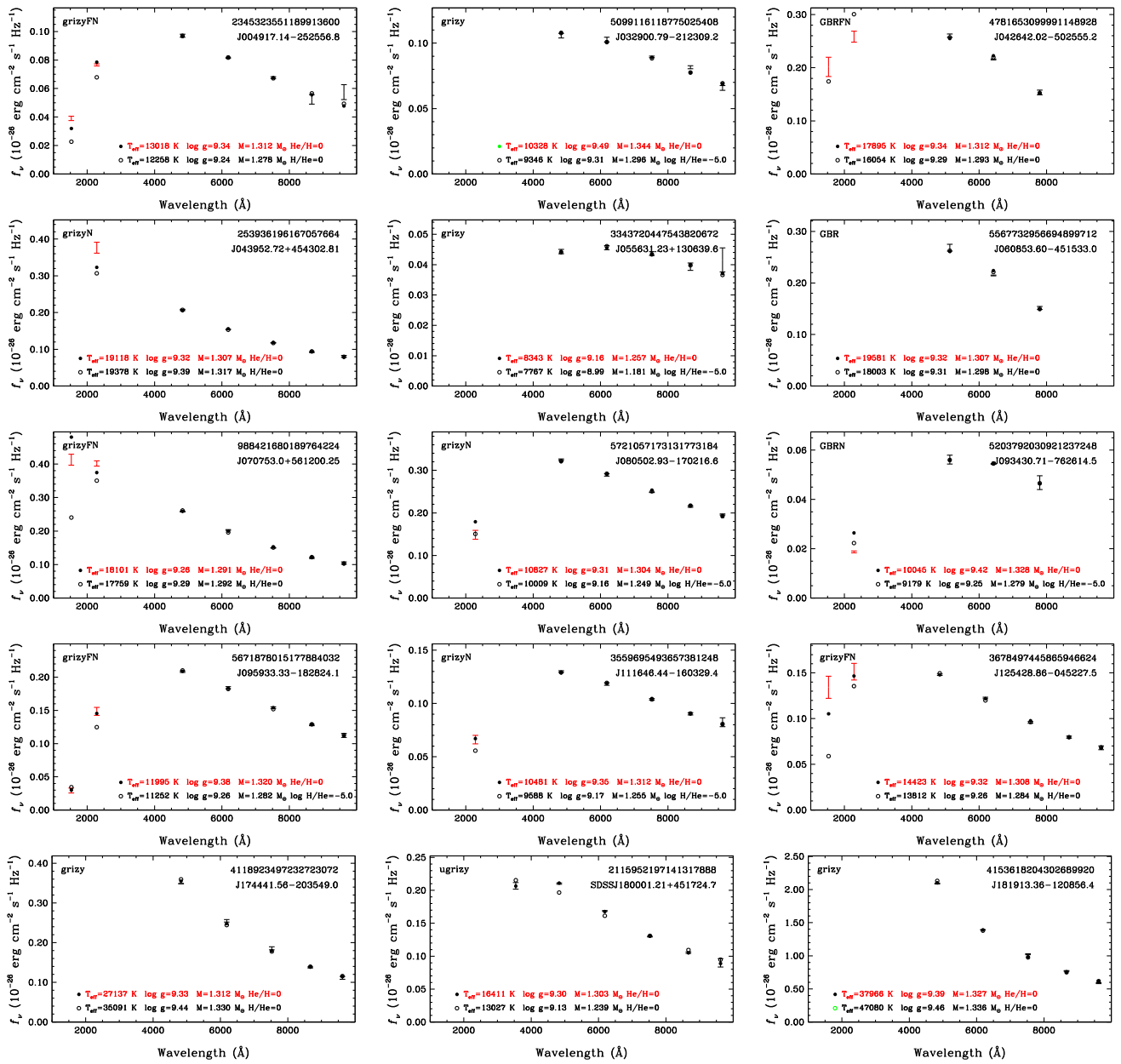


**Figure 9.** Model atmosphere fits to 15 ultramassive white dwarf candidates without follow-up spectroscopy. The symbols are the same as in Fig. 4. The best-fitting parameters are for CO cores.

binary mergers can explain both the observed incidence of magnetism and the mass distribution of highly magnetic white dwarfs.

Interestingly, out of the 10 ultramassive white dwarfs with follow-up spectroscopy, 4 are likely magnetic (see Section 4.3.2). As discussed above, one of these stars, J2211 + 1136, also displays a large transverse velocity, further providing evidence for its merger origin.

Merger populations can also reveal themselves through rapid rotation. Modelling the evolution of the remnants of double white dwarf mergers, Schwab (2021) estimate rotation periods of 10–20 min for most remnants on the white dwarf cooling track. However, they find that the most massive white dwarfs with  $M \geq 1.2 M_{\odot}$  likely have shorter rotation periods of 5–10 min.

Only one of the ultramassive white dwarf candidates in our sample has a rotation measurement available. Pshirkov et al. (2020) found

a rotation period of 353 s for the DBA white dwarf J1832 + 0856, which is entirely consistent with the simulations by Schwab (2021). Hence, J1832 + 0856 has likely formed through binary evolution as well. Combining the results from these three different techniques shows that at least 8 of the 25 ultramassive white dwarfs in our sample are likely to have a binary origin.

### 5.3 Future prospects

There are several factors that contribute to the rarity of ultramassive white dwarfs in the solar neighbourhood. The steep slope of the initial-mass function (Salpeter 1955) means that their progenitor main-sequence stars are rare. In addition, given their smaller radii, ultramassive white dwarfs are fainter than average, hence harder to find in magnitude limited surveys. The latent heat from crystallization

**Table 3.** Physical parameters of the photometry only sample assuming ONe or CO cores. All solutions above  $1.29 M_{\odot}$  for ONe core models and above  $1.334 M_{\odot}$  for CO core models are extrapolated.

Object	Composition	$T_{\text{eff}}$ (K)	ONe core Mass ( $M_{\odot}$ )	ONe core Cooling age (Gyr)	CO core Mass ( $M_{\odot}$ )	CO core Cooling age (Gyr)
J004917.14-252556.81	H	$13020 \pm 460$	$1.263 \pm 0.011$	$1.94 \pm 0.08$	$1.312 \pm 0.010$	$1.72 \pm 0.09$
...	He	$12260 \pm 390$	$1.236 \pm 0.011$	$2.06 \pm 0.08$	$1.278 \pm 0.012$	$1.68 \pm 0.07$
J032900.79-212309.24	H	$10330 \pm 290$	$1.305 \pm 0.010$	$2.32 \pm 0.06$	$1.344 \pm 0.008$	$1.87 \pm 0.09$
...	$\log \text{H/He} = -5$		$9350 \pm 250$	$1.256 \pm 0.011$	$2.74 \pm 0.07$	$1.296 \pm 0.010$
J042642.02-502555.21	H	$17900 \pm 1570$	$1.264 \pm 0.019$	$1.30 \pm 0.16$	$1.312 \pm 0.016$	$1.08 \pm 0.16$
...	He	$16050 \pm 1680$	$1.253 \pm 0.031$	$1.51 \pm 0.21$	$1.293 \pm 0.028$	$1.15 \pm 0.19$
J043952.72 + 454302.81	H	$19120 \pm 630$	$1.258 \pm 0.008$	$1.18 \pm 0.06$	$1.307 \pm 0.007$	$0.96 \pm 0.06$
...	He	$19380 \pm 1300$	$1.283 \pm 0.019$	$1.24 \pm 0.11$	$1.317 \pm 0.014$	$0.81 \pm 0.10$
J055631.17 + 130639.78	H	$8340 \pm 260$	$1.207 \pm 0.021$	$3.33 \pm 0.12$	$1.257 \pm 0.023$	$3.34 \pm 0.18$
...	$\log \text{H/He} = -5$		$7770 \pm 170$	$1.157 \pm 0.029$	$3.53 \pm 0.07$	$1.181 \pm 0.029$
J060853.60-451533.03	H	$19580 \pm 1910$	$1.258 \pm 0.021$	$1.13 \pm 0.16$	$1.307 \pm 0.019$	$0.92 \pm 0.17$
...	He	$18000 \pm 2800$	$1.259 \pm 0.047$	$1.31 \pm 0.29$	$1.298 \pm 0.040$	$0.96 \pm 0.26$
J070753.00 + 561200.25	H	$18100 \pm 350$	$1.240 \pm 0.005$	$1.23 \pm 0.04$	$1.291 \pm 0.005$	$1.06 \pm 0.04$
...	He	$17760 \pm 580$	$1.252 \pm 0.009$	$1.31 \pm 0.06$	$1.292 \pm 0.009$	$0.98 \pm 0.05$
J080502.93-170216.57	H	$10830 \pm 110$	$1.254 \pm 0.004$	$2.40 \pm 0.03$	$1.304 \pm 0.003$	$2.20 \pm 0.03$
...	$\log \text{H/He} = -5$		$10010 \pm 120$	$1.213 \pm 0.004$	$2.70 \pm 0.04$	$1.249 \pm 0.006$
J093430.71-762614.48	H	$10050 \pm 1350$	$1.284 \pm 0.055$	$2.47 \pm 0.35$	$1.328 \pm 0.047$	$2.11 \pm 0.50$
...	$\log \text{H/He} = -5$		$9180 \pm 1050$	$1.238 \pm 0.052$	$2.86 \pm 0.33$	$1.279 \pm 0.051$
J095933.33-182824.16	H	$12000 \pm 180$	$1.273 \pm 0.005$	$2.12 \pm 0.03$	$1.320 \pm 0.004$	$1.83 \pm 0.04$
...	$\log \text{H/He} = -5$		$11250 \pm 190$	$1.241 \pm 0.007$	$2.31 \pm 0.05$	$1.282 \pm 0.007$
J111646.44-160329.42	H	$10480 \pm 170$	$1.264 \pm 0.007$	$2.45 \pm 0.05$	$1.312 \pm 0.006$	$2.21 \pm 0.07$
...	$\log \text{H/He} = -5$		$9590 \pm 160$	$1.218 \pm 0.007$	$2.82 \pm 0.05$	$1.255 \pm 0.010$
J125428.86-045227.48	H	$14420 \pm 390$	$1.258 \pm 0.008$	$1.71 \pm 0.06$	$1.308 \pm 0.007$	$1.52 \pm 0.06$
...	He	$13810 \pm 310$	$1.243 \pm 0.009$	$1.79 \pm 0.05$	$1.284 \pm 0.009$	$1.43 \pm 0.04$
J174441.56-203549.05	H	$27140 \pm 890$	$1.271 \pm 0.008$	$0.65 \pm 0.06$	$1.312 \pm 0.008$	$0.43 \pm 0.04$
...	He	$35090 \pm 1410$	$1.317 \pm 0.009$	$0.45 \pm 0.05$	$1.330 \pm 0.007$	$0.18 \pm 0.03$
J180001.21 + 451724.7	H	$16410 \pm 290$	$1.253 \pm 0.003$	$1.44 \pm 0.03$	$1.303 \pm 0.004$	$1.26 \pm 0.04$
...	He	$13030 \pm 180$	$1.206 \pm 0.004$	$1.85 \pm 0.04$	$1.239 \pm 0.006$	$1.57 \pm 0.03$
J181913.36-120856.44	H	$37970 \pm 1940$	$1.305 \pm 0.009$	$0.37 \pm 0.03$	$1.327 \pm 0.006$	$0.12 \pm 0.03$
...	He	$47080 \pm 1000$	$1.327 \pm 0.006$	$0.29 \pm 0.01$	$1.336 \pm 0.004$	$0.02 \pm 0.01$

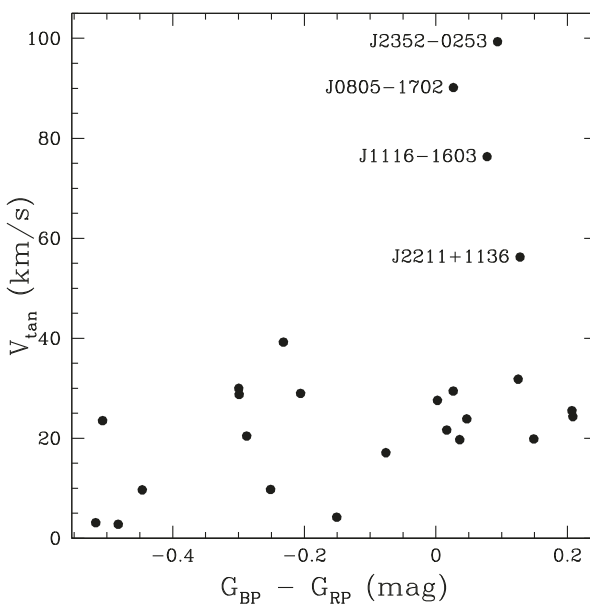


**Figure 10.** *Gaia* colours (from DR2) and tangential velocities (from EDR3) of our sample of ultramassive white dwarf candidates presented in Table 1. The four velocity outliers are labelled.

can keep these white dwarfs brighter for longer, but once they reach the Debye cooling regime, they cool rapidly and disappear from view. Their numbers are significantly depleted for ages older than a few Gyrs.

*Gaia* DR2 has provided us with a sample of 25 ultramassive white dwarf candidates with  $M \sim 1.3 M_{\odot}$  and within 100 pc. With increased precision in parallax and photometry, future *Gaia* data releases may reveal additional ultramassive white dwarfs in the solar neighbourhood.

The Rubin Observatory's 10-year Legacy Survey of Space and Time (LSST) will find millions of white dwarfs, which will include many ultramassive white dwarfs as well. An exciting prospect with these discoveries is that the time-series photometry from the LSST can be used to measure the rotation periods of ultramassive white dwarfs, and to identify rapidly rotating systems that likely formed through binary mergers. Such measurements can also constrain, as a function of mass, the fraction of single white dwarfs that form through mergers.

## ACKNOWLEDGEMENTS

We acknowledge enlightening discussions with our late colleague G. Fontaine regarding the cooling sequences discussed in this work. MK thanks E. Baron for useful discussions.

This work is supported in part by the NSF under grant AST-1906379, the NSERC Canada, and by the Fund FRQ-NT (Québec).

S.B. acknowledges support from the Laboratory Directed Research and Development program of Los Alamos National Laboratory under project number 20190624PRD2.

Based on observations obtained at the Gemini Observatory, which is operated by the Association of Universities for Research in Astronomy, Inc., under a cooperative agreement with the NSF on behalf of the Gemini partnership: the National Science Foundation (United States), National Research Council (Canada), CONICYT (Chile), Ministerio de Ciencia, Tecnología e Innovación Productiva (Argentina), Ministério da Ciência, Tecnologia e Inovação (Brazil), and Korea Astronomy and Space Science Institute (Republic of Korea).

## DATA AVAILABILITY

The data underlying this article are available in the MWDD at <http://www.montrealwhitedwarfdatabase.org> and in the Gemini Observatory Archive at <https://archive.gemini.edu>, and can be accessed with the program numbers GN-2020A-DD-113 and GN-2020B-FT-107.

## REFERENCES

Barstow M. A., Jordan S., O'Donoghue D., Burleigh M. R., Napiwotzki R., Harrop-Allin M. K., 1995, *MNRAS*, 277, 971

Bauer E. B., Schwab J., Bildsten L., Cheng S., 2020, *ApJ*, 902, 93

Bédard A., Bergeron P., Brassard P., Fontaine G., 2020, *ApJ*, 901, 93

Bergeron P., Saffer R. A., Liebert J., 1992, *ApJ*, 394, 228

Bergeron P., Dufour P., Fontaine G., Coutu S., Blouin S., Genest-Beaulieu C., Bédard A., Rolland B., 2019, *ApJ*, 876, 67

Blouin S., Dufour P., Allard N. F., Kilic M., 2018, *ApJ*, 867, 161

Blouin S., Dufour P., Thibeault C., Allard N. F., 2019, *ApJ*, 878, 63

Briggs G. P., Ferrario L., Tout C. A., Wickramasinghe D. T., Hurley J. R., 2015, *MNRAS*, 447, 1713

Caiazzo I. et al., 2020, *ApJ*, 901, L14

Camisassa M. E. et al., 2019, *A&A*, 625, A87

Chambers K. C. et al., 2016, preprint ([arXiv:1612.05560](https://arxiv.org/abs/1612.05560))

Chandrasekhar S., 1931, *ApJ*, 74, 81

Cheng S., Cummings J. D., Ménard B., 2019, *ApJ*, 886, 100

Cheng S., Cummings J. D., Ménard B., Toonen S., 2020, *ApJ*, 891, 160

Coutu S., Dufour P., Bergeron P., Blouin S., Loranger E., Allard N. F., Dunlap B. H., 2019, *ApJ*, 885, 74

Cummings J. D., Kalirai J. S., Tremblay P. E., Ramirez-Ruiz E., Bergeron P., 2016, *ApJ*, 820, L18

Dahn C. C., Bergeron P., Liebert J., Harris H. C., Canzian B., Leggett S. K., Boudreault S., 2004, *ApJ*, 605, 400

Deacon N. R. et al., 2009, *MNRAS*, 397, 1685

Dufour P., Bergeron P., Fontaine G., 2005, *ApJ*, 627, 404

Dufour P. et al., 2007, *ApJ*, 663, 1291

Dufour P., Blouin S., Coutu S., Fortin-Archambault M., Thibeault C., Bergeron P., Fontaine G., 2017, in Tremblay P. E., Gaensicke B., Marsh T., eds, ASP Conf. Ser. Vol. 509, 20th European White Dwarf Workshop. Astron. Soc. Pac., San Francisco, p. 3

Ferrario L., Vennes S., Wickramasinghe D. T., Bailey J. A., Christian D. J., 1997, *MNRAS*, 292, 205

Gagné J., Fontaine G., Simon A., Faherty J. K., 2018, *ApJ*, 861, L13

Gaia Collaboration et al., 2018, *A&A*, 616, A10

Gaia Collaboration, Brown A. G. A., Vallenari A., Prusti T., de Bruijne J. H. J., Babusiaux C., Biermann M., 2020, *A&A*, preprint ([arXiv:2012.01533](https://arxiv.org/abs/2012.01533))

Gates E. et al., 2004, *ApJ*, 612, L129

Genest-Beaulieu C., Bergeron P., 2019, *ApJ*, 882, 106

Gentile Fusillo N. P. et al., 2019, *MNRAS*, 482, 4570

Giammichele N. et al., 2018, *Nature*, 554, 73

Gianninas A., Bergeron P., Ruiz M. T., 2011, *ApJ*, 743, 138

Hamada T., Salpeter E. E., 1961, *ApJ*, 134, 683

Harris H. C. et al., 2001, *ApJ*, 549, L109

Hollands M. A. et al., 2020, *Nat. Astron.*, 4, 663

Kilic M., Bergeron P., Kosakowski A., Brown W. R., Agüeros M. A., Blouin S., 2020, *ApJ*, 898, 84

Lindegren L. et al., 2018, *A&A*, 616, A2

McCeery J. et al., 2020, *MNRAS*, 499, 1890

Miyaji S., Nomoto K., Yokoi K., Sugimoto D., 1980, *PASJ*, 32, 303

Murai T., Sugimoto D., Hōshi R., Hayashi C., 1968, *Progress Theoret. Phys.*, 39, 619

Nomoto K., 1987, *ApJ*, 322, 206

Pshirkov M. S. et al., 2020, *MNRAS*, 499, L21

Salpeter E. E., 1955, *ApJ*, 121, 161

Schmidt G. D., Bergeron P., Liebert J., Saffer R. A., 1992, *ApJ*, 394, 603

Schwab J., 2021, *ApJ*, 906, 53

Takahashi K., Yoshida T., Umeda H., 2013, *ApJ*, 771, 28

Temmink K. D., Toonen S., Zapartas E., Justham S., Gānsicke B. T., 2020, *A&A*, 636, A31

Tout C. A., Wickramasinghe D. T., Liebert J., Ferrario L., Pringle J. E., 2008, *MNRAS*, 387, 897

Tremblay P.-E. et al., 2019, *Nature*, 565, 202

Tremblay P. E. et al., 2020, *MNRAS*, 497, 130

Wegg C., Phinney E. S., 2012, *MNRAS*, 426, 427